Journal of Physics: Conference Series **190** (2009) 012004 doi:10.1088/1742-6596/190/1/012004

XANES spectra of transition metal compounds

Frank M. F. de Groot

Inorganic Chemistry and Catalysis, Utrecht University,
Sorbonnelaan 16, 3584 CA Utrecht, Netherlands

Abstract An overview is given of the interactions that determine the XANES spectral shapes of transition metal compounds. The interactions are divided into ground state effects, final state effects and transition effects. The metal L edges, metal K edges and ligand K edges are analysed with respect to these interactions. The importance of XANES is partly due to its wide versatility in measurement conditions. XANES spectra can be measured using a number of sample environments, ranging from vacuum to ambient pressures for soft x-rays and up to extreme conditions with hard X-rays. These in-situ XANES spectra can be measured with a spatial resolution of 10 to 30 nm. XANES spectral shapes can be used as resonant channels in resonant photoemission, resonant x-ray emission or resonant diffraction experiments. This gives rise to a large number of resonant techniques that also allow the detection of site, valence, spin and symmetry selective XANES spectra and/or XANES spectra revealing information with a resolution better than its lifetime broadening.

1. Introduction

This short review deals with the analysis of X-ray Absorption Near Edge Spectroscopy (XANES) spectra of transition metal systems. The main focus is on the various interactions that determine the XANES spectral shapes. In addition, it is discussed how one can derive useful information from XANES, where it is noted that to derive this information it is not always necessary to completely understand all features of the spectral shape. XANES spectra are usually measured by the absorption of X-rays. In addition, there are two alternative routes to measure exactly the same XANES spectrum: (i) Electron Energy Loss Spectroscopy (EELS) and (ii) X-ray Raman scattering or in other words X-ray Energy Loss Spectroscopy (XELS). In EELS a high-energy electron is inelastically scattered where the energy loss equals the core level binding energy. At low momentum transfer this identifies with the XANES spectral shape. XELS is the analogue experiments but now with high energy X-rays. Both EELS and XELS have the option to modify the selection rules via finite momentum transitions. EELS and XELS typically cover the soft X-ray energy range, while XAS also includes the hard X-ray metal K edges.

The crucial aspects that determine the amount of detail in the XANES spectra are the lifetime broadening of the core hole plus the experimental resolution. Concerning the transition metal L edges an important step was made in eighties when the resolution of soft XAS reached ~0.2 eV in 1987-1989 with the development of the SX700 and DRAGON monochromators[1,2]. An intrinsic limitation is the lifetime broadening which amounts to ~0.2 eV for metal L_3 edges and ligand K edges and to ~1.5 eV for metal K edges.

2. Interpretation of the spectral shapes

The XANES spectral shape is given by the Fermi golden rule. The core electron is excited to an empty state, starting from the lowest empty state. As such, one essentially probes the empty Density of States (DOS). One can make the following approximations to calculate the XANES spectral shape:

- Ground state DOS approximation (0,0): It is assumed that the XANES spectrum identifies with the ground state DOS, as calculated, for example, by density functional theory (DFT). The ground state DOS approximation can be written as (0,0) to indicate no core hole and no extra electron[2].
- Final state DOS approximation (1,1): It is assumed that the final state DOS should be used instead, where (1,1) stands for one core hole plus one extra valence electron originating from the core hole and indicated as blue electron.
- Other approximations for core hole and blue electron are the Slater transition state approximation, indicated as (½,½), and other partial hole calculations. Recently, the relative amount of core hole has been approximated from DFT calculations[3].

We will below, very briefly, introduce some of the major approximations and complications in the actual XANES calculations. It is highly dependent on the system and the specific edge which effects are visible in the spectrum. If a process has an energy effect of less than the lifetime broadening, it is not visible in the corresponding XANES spectra. The approximations are divided into ground state effects (G1 to G5), final state effects (F1 to F5) and transition effects (T1 to T4), where it is noted that these divisions are for some effects partly artificial. We assume that the ground state is calculated with a DFT based code such as the band structure codes PARATEC[4, 5], WIEN2K[6], CASTEP[7] or real space multiple scattering codes such as FDMNES[8], FEFF[9], CONTINUUM[10] and MXAN[11]. Within molecule based DFT codes (including STOBE[12], ADF[13] and ORCA[14]) these effects appear in a modified fashion, not further discussed in this paper. The ground state effects include:

G1. *Exchange interactions* and spin-polarization, i.e. the intra- and inter-atomic spin-spin correlations
G2. *Orbital polarization*, and the intra-atomic 3d3d multipole interactions
G3. *3d spin-orbit coupling*, with a strength between 10 and 100 meV, often (but not always) quenched by translation symmetry or crystal field symmetry.
G4. *3d3d correlation energy* (U), i.e. the effects due to charge fluctuations in the 3d occupation. This effect is included in LDA+U calculations and Dynamical Mean Field Theory (DMFT).
G5. *Charge transfer channels* (Δ), i.e. the effects due inter-atomic charge excitations/fluctuations.

The final state rule is assumed to hold for many spectra, implying the assumption that the XANES spectrum is given in the (1,1) limit. This implies the inclusion of the core hole that is separated into five effects below. These final state effects include:

F1. *Core hole potential*, included in most DFT codes, within reciprocal space calculations within a super-cell to minimize core hole-core hole interactions.
F2. *Core hole spin-orbit coupling*, yielding a distinction between the L_3 and L_2 edge. Without the effects mentioned in F4 and F5 and without the inclusion of the ground state spin-orbit coupling (G3), the L_3 and L_2 spectra are identical with a ratio of 2:1.
F3. *Core hole induced charge transfer effects*, including shake-up and Rydberg states. This effect includes the transitions to orbitals that are higher in energy in the ground state and are coupled into combined states. Due to the core hole potential and the different localization of orbitals, the final state ordering of orbitals is strongly modified with the 3d orbitals shifted down.
F4. *Core hole – valence hole exchange*. The 2s and 3s core holes have an exchange interaction with the polarized 3d states that can be indicated with a G_1 Slater integral. The 2p and 3p core holes in addition have a higher-order exchange interaction indicated with G_3.
F5. *Core hole – valence hole multipole interactions*. The 2p and 3p core holes have a dipole-dipole interaction with the 3d holes that can be described with the F_2 Slater integral. Together F4 and F5 constitute the so-called multiplet effect.

To date no general program exists that includes all the effects mentioned above in an ab-initio manner. Closest to a generalized ab-initio approach are the routes that start with a ground state DFT calculation, then project the wave functions to a (small) cluster and subsequently solve the final state effects for such cluster. The methods that are being developed by Kruger[15], Uozumi[16], Ikeno[17] and Haverkort[18] follow such procedure.

Having calculated the initial state or final state DOS, one has to also calculate the transition strength of the x-ray induced transition. Usually this calculation assumes the dipole approximation, yielding the selection rules $\Delta J=+1,-1$ or 0, or alternatively if spin-orbit couplings are neglected $\Delta L=+1,-1$ and $\Delta S=0$. Some transition effects include:

T1. *Matrix elements*: The matrix elements are energy-dependent, though usually they follow a smooth function for delocalized final states. With localized final states, strongly varying matrix elements are possible.
T2. *Quadrupole transitions*: The metal K edges are related to 1s4p transitions. Below the empty 4p states one finds the partly empty 3d-band. Quadrupole transitions allow direct 1s3d transitions.
T3. *Quadrupole-dipole mixing*: In systems without inversion symmetry the even (4p) and odd (3d) orbitals can mix with each other, yielding effects due to quadrupole-dipole mixing.

2.1.1. Consequences for the XANES spectra of transition metal compounds

Ligand K edges contain a 1s core hole, implying that the effects F2, F4 and F5 are absent. Because of the screening effects in the final state, ligand K edges are often close to the (0,0) limit, allowing ground state DFT calculations. Because of the life-time broadening of ~0.3 eV the fine details of the ground state interactions are not, easily, visible.

Metal K edges have a lifetime broadening of ~1.5 eV implying that the 3d-band is often only visible as a feature with only one or two peaks, blurring much detail of the DOS features. The pre-edges are further discussed below in the context of RIXS. The edge structure can usually be simulated with any DFT code[19].

Metal L edges have their characteristic multiplet structure that has been simulated in detail using crystal field multiplet calculations. Divalent transition metal oxides and halides can be simulated well with a crystal field multiplet approach[20, 21]. More covalent systems are stronger affected by metal-to-ligand charge transfer effects and need a charge transfer multiplet calculation with two or more configurations[22, 23]. Systems with large π-bonding need the additional inclusion of ligand-to-metal charge transfer channels[24].

3. Deriving useful information from XANES spectra

The detailed interpretation of XANES spectra is not necessarily equivalent with the derivation of useful information from XANES spectra. Often one can derive very useful information from more qualitative analysis without the need for a very detailed theoretical understanding. In some cases, it is already important to derive the (average) *valence* of a system. Figure 1 shows the average valence of iron in a Fe/ZSM5 catalyst measured with (conversion) electron yield[25]. The iron valence approaches a steady state of 2.95 in oxygen. Switching to a He atmosphere changes the average valence in a few minutes to ~2.65, indicating that valence-sensitive materials behave completely different in air and in vacuum.

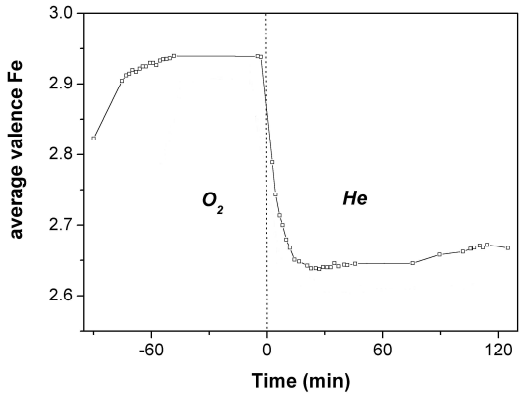

***Figure 1**. Determination of the average valence of a Fe/ZSM5 catalyst, using the iron L_3 edge.*

In addition to the valence, the metal L edge provides information on the *spin state* and the *crystal field strength*. Polarization dependent experiments on ordered systems can enhance this information and allow the determination of the *energies of all 3d-orbitals*. For example, Gambardella et al. used polarization dependence and MCD to determine the 3d orbital energies of a Fe-TPA complex at a metal interface before and after reaction with oxygen[26]. The L edge shape directly allows the assignment of high-spin and low-spin ground states. In some cases, the ground state is found to have *intermediate spin* or a *mixed spin* ground state[27]. The *degree of covalence* can be determined from the relative contributions of the various configurations and this covalence analysis can be separated into various symmetries. In cubic symmetry this provides the difference in localisation of t_{2g} respectively e_g electrons, the so-called *differential orbital covalency*[28].

Ligand K edges show essentially the empty DOS and the analysis of the ligand p-states that hybridise with the metal 3d-states directly yield the *covalence* of these 3d-states. This has been shown for bulk oxides[29] and for coordination compounds[30].

Metal K edges are used to determine the metal valence. The pre-edges also reveal the metal valence and, in addition, the pre-edge intensity is determined by the amount of dipole character in the pre-edge, which in turn is determined by the site symmetry of the absorbing sites. The combination of pre-edge intensity and energy yields a very useful characterization tool that is often used[31-33]. Recent RIXS experiments performed at the pre-edge energies reveal that the pre-edge spectral shape is more complex than usually assumed, an issue that is discussed below.

4. Sample environment, space & time resolution

XANES spectra are measured on atoms, molecules, bulk solids, surfaces, adsorbates and nanoparticles. Recently much progress was made to extend the soft X-ray XANES measurements on small clusters and in the liquid state, including dissolved molecular complexes and proteins. An important advantage of XANES spectra is that they allow element selective information on essentially any system under study. Soft X-ray XANES spectra are traditionally measured in vacuum, but more and more in-situ reactor cells become available, allowing the in-situ measurements of active systems, including catalysts, batteries and fuel cells. Hard X-ray XANES have more options including high-pressures and high temperatures.

Time-resolved XANES includes experiments that track a process in minutes to hours, for example synthesis reactions or catalyst poisoning and deactivation. These can also be studied in the milliseconds to seconds' time range using fast experiments, for example a dispersive beamline in combination with a stop-flow reaction chamber. The nanosecond to microsecond time range usually needs an electromagnetic trigger and for example time-resolved magnetic effects can be studied.

Picosecond time-resolved experiments are performed in pump-probe mode, for example studying the spin-state dynamics of excited states[34]. Experiments faster than the synchrotron bunch length need time-slicing, which allows femtosecond experiments though with few photons. (Soft) X-ray FEL beam lines will allow femtosecond experiments, though with the side effect of sample destruction

Spatial resolution in the micron range can be obtained by focused beams and/or pin-holes. Scanning Transmission X-ray Microscopes (STXM) reach 10 nm resolution for soft X-rays and 100 nm for the hard X-rays. By combining a STXM microscope with an in-situ nanoreactor we have tracked catalyst synthesis and activation (reduction) and also the catalytic reaction of iron-oxide based Fischer-Tropsch catalysts[35, 36]. The nanoreactor allows measurements up to 2 bar and 500 Celsius, which is very interesting for experiments in catalysis, fuel cells, hydrogen storage, aerosols, etc.

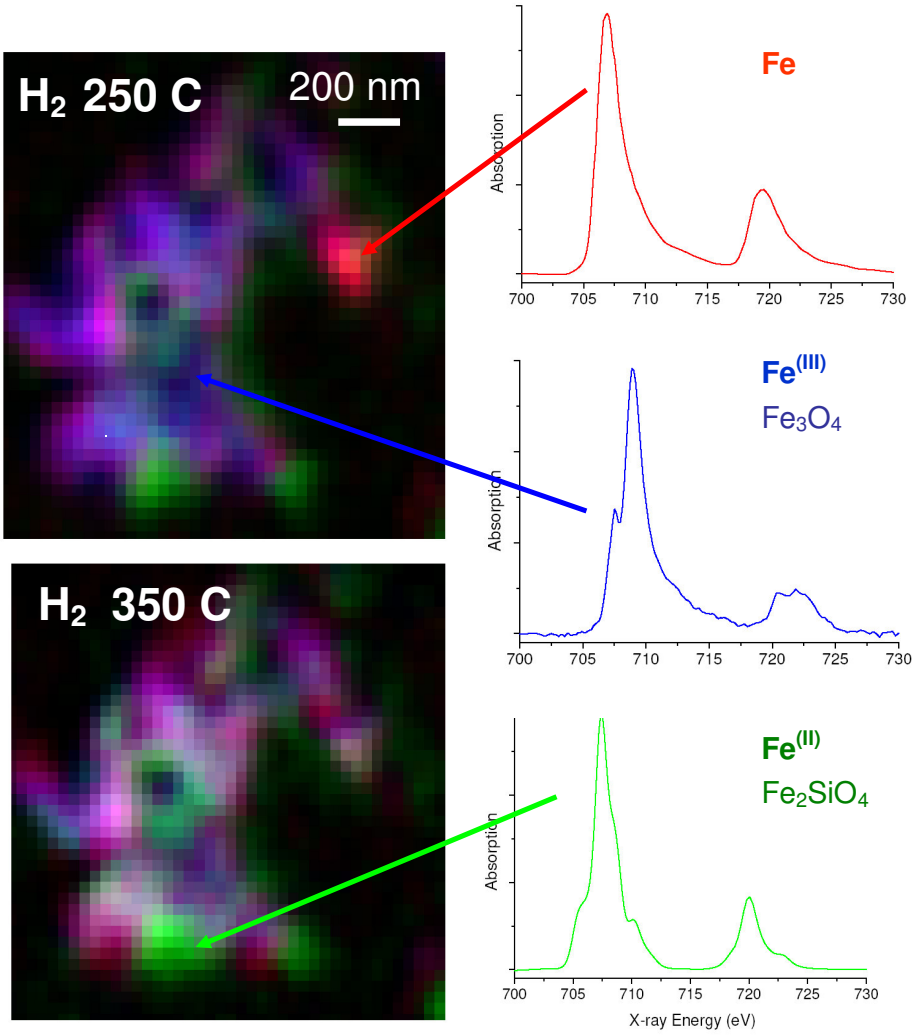

Figure 2. *Chemical component images of the catalyst particle, showing the spatial distribution of the different iron species (left) with Fe (red), Fe^{2+} (green) and Fe3O4 (blue) of an iron Fischer-Tropsch catalyst in 1 bar H2 at 250 C and 350 C. The iron L edge spectra on the left are integrated over a small area as indicated by the arrows.*

Figure 2 shows that at 250 C this iron based Fischer-Tropsch catalyst is very inhomogeneous on a ~100 nm scale. Some areas are already reduced to iron metal wile other are still non-reduced Fe3O4 pieces. At higher temperatures, the catalysts becomes more homogeneous[35, 36].

5. Using XANES for resonant experiments

The XANES spectral shape can be used to perform resonant experiments, where essentially the edge contrast and signal enhancement is used. Resonant experiments include:

R1. Resonant photoemission (RPES) and Auger (RAES)
R2. Resonant X-ray emission (RXES)
R3. Resonant or Anomalous Diffraction/Scattering

Resonant photoemission is a well known technique for the metal 2p and 3p states. One can measure a large range of combinations of valence and core states for the resonant phenomena. The most common techniques are 2p3d3d resonant photoemission, a process that interferes with direct 3d photoemission. In addition 2p3p3dB RPES and 2p3s3d RPRES determine the resonant 3p and 3s PES spectra. Resonant Auger spectra involve only core electrons, for example 2p3p3p RAES, etc. No direct photoemission channel interferes in case of RAES[37].

RXES or Resonant Inelastic X-ray Scattering (RIXS) experiments have made an enormous development over the last years due to the availability of dedicated beamlines with drastically improved resolution and count rates. Further improvements are expected over the next years. In the soft X-ray range the 2p3d RIXS experiments can be used to track the elementary excitations of the system, including their momentum distribution. The present overall resolution of such valence band RIXS experiments is 100 meV, allowing the mapping, for example (bi)magnon, dd and charge transfer excitations[38]. The 3p3d RIXS allows even higher energy resolution, though with less possibilities for q-mapping. In addition 2p3s RIXS experiments can be used for enhanced information for core level analysis.

Hard X-ray RIXS experiments include 1s2p and 1s3p RIXS surfaces that can be measured with 300 meV overall resolution, allowing the determination of spectral details with a resolution much better than the 1s core hole lifetime of ~1.5 eV. 1sVB RIXS has weak intensity; it reveals the low-loss excitations such as the dd-excitations with modified cross sections that are sensitive the dipole-quadrupole mixing of the states. A further spectroscopic option are the XES channels from the shallow 2s states of the C, N or O ligand due to overlap with the metal 4p states[39, 40].

One can use RIXS, RPES or RAES to measure site selective, spin selective or valence selective X-ray absorption spectra. For some edges it is possible to effectively remove the lifetime broadening and effectively measure the K pre-edge without its lifetime broadening. Recent experiments using 1s2p RIXS channel revealed new peaks in a range of systems. A clear example of these High Energy Resolved Fluorescence Detection (HERFD) spectra are the spectra of low-spin $3d^6$ systems that clearly show the (single) quadrupole peak combined with the non-local dipole peak. This non-local dipole peak is large only if three conditions are fulfilled: (i) ligand-coupled metal-metal interactions, (ii) a high-valent metal and (iii) the presence of local inversion symmetry[41, 42]. The presence of an intense non-local peak significantly modifies our understanding of the metal K pre-edge structures, for example the integration of the pre-edge intensity and its correlation with site symmetry. A problem in normal metal K edge XANES is that due to the large life time broadening, the intensity of the non-local peak is buried under the leading edge structure, making it difficult to distinguish. RIXS experiments reveal the presence of the non-local peak by the dispersion of the RIXS features[41].

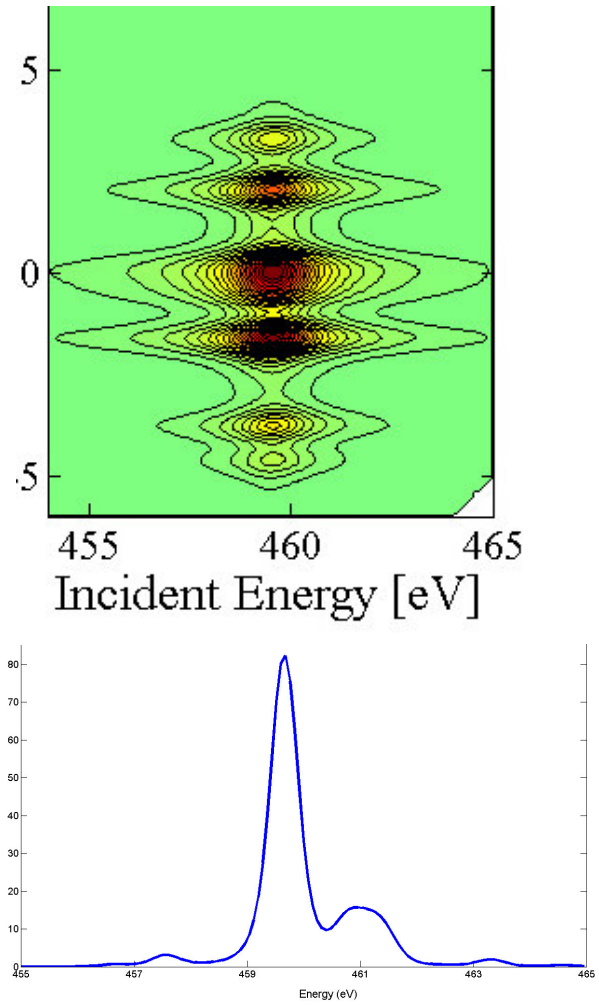

Figure 3. *(top) Calculation of the 2p4d RIXS. All energies have been shifted by 7000 eV. (bottom) The pre-edge region of the theoretical HERFD-XANES spectrum of LaF_3, which is derived from a cross section through the RIXS plane.*

.

Recent HERFD-XANES spectra of the 2p XANES of La systems also revealed many new peaks present in the pre-edge region. Instead of the single quadrupole 2p4f peak, a series of pre-edge features are visible in the HERFD-XANES spectra, measured with 0.3 eV overall resolution[43]. It turns out that these are not genuine XANES features, but instead they are peaks induced by the strong multiplet effects in the 4d final state that is used for the HERFD-XANES detection. This is nicely visible in figure 3, where HERFD-XANES identifies with a 45 degrees cross section through the series of RIXS features that all are related to a single excitation at ~7460 eV

6. Future perspectives

The recently developed nanoreactor for in-situ STXM experiments on catalytic systems can be expected to yield a range of very interesting new results in catalysis, electrochemistry, materials science and environmental science. Further developments are expected to yield reactors for liquids and, possibly, nanoreactors for STXM tomography. The development of 10 nm STXM beamlines that would be capable to detect the metal K edges will further enlarge the possibilities for experiments

under extreme conditions. It is obvious that time-resolved measurements in the femtosecond domain will gain much from the new X-FEL experiments.

RIXS reveals many new details in the XANES spectra and even more in the full analysis of the 2D RIXS planes. The resolution (in combination with detection efficiency) of RIXS is still improving, which promises many new discoveries in the next years. This is true both for soft- x-ray RIXS and hard x-ray RIXS. Soft x-ray RIXS holds many promises for revealing the q-dependence of elementary excitations in solids, but possibly even more for nanoparticles and (bio-)molecules in the liquid state. Hard X-ray RIXS does not yield the same resolution, however it is possible to measure hard x-ray RIXS spectra under extreme conditions. An additional new asset of hard x-ray RIXS studies is the detection of RIXS-MCD effect. Measuring the angular dependence of the pre-edge RIXS reveals its partial dipolar, respectively quadrupole nature[41, 44]. The quadrupole peaks can also be strongly enhanced by using the Borrmann effect[45]. It would be very interesting to understand (and use) the various options for the combination of XANES with inelastic scattering as well as with diffraction. Much has still to be discovered in these areas.

Acknowledgements

F.d.G. acknowledge financial support from the Netherlands National Science Foundation (NWO/VICI program).

References

1. C. T. Chen and F. Sette, Rev. Sci. Instrum. **60**, 1616 (1989).
2. L. Petterson, (priv. comm.) (2009).
3. V. Mauchamp, M. Jaouen, and P. Schattschneider, Phys. Rev. B **79**, 16 (2009).
4. D. Cabaret, F. Mauri, and G. S. Henderson, Phys. Rev. B **75** (2007).
5. E. Gaudry, D. Cabaret, P. Sainctavit, C. Brouder, F. Mauri, J. Goulon, and A. Rogalev, J. Phys. Cond. Matt. **17**, 5467 (2005).
6. K. Schwarz, P. Blaha, and G. K. H. Madsen, Comp. Phys. Comm. **147**, 71 (2002).
7. V. Milman, B. Winkler, J. A. White, C. J. Pickard, M. C. Payne, E. V. Akhmatskaya, and R. H. Nobes, Int. J. Quant. Chen. **77**, 895 (2000).
8. Y. Joly, J. Synchr. Rad. **10**, 58 (2003).
9. J. J. Rehr and R. C. Albers, Rev. Mod. Phys. **72**, 621 (2000).
10. Z. Y. Wu, D. C. Xian, T. D. Hu, Y. N. Xie, Y. Tao, C. R. Natoli, E. Paris, and A. Marcelli, Phys. Rev. B **70**, 33104 (2004).
11. M. Benfatto, S. Della Longa, and C. R. Natoli, J. Synchr. Rad.**10**, 51 (2003).
12. C. Kolczewski and K. Hermann, Theo. Chem. Acc. **114**, 60 (2005).
13. G. Fronzoni, M. Stener, P. Decleva, M. de Simone, M. Coreno, P. Franceschi, C. Furlani, and K. C. Prince, J. Phys. Chem. A **113**, 2914 (2009).
14. S. D. George, T. Petrenko, and F. Neese, J. Phys. Chem. A **112**, 12936 (2008).
15. P. Kruger and C. R. Natoli, Phys. Rev. B **70** (2004).
16. A. Agui, T. Uozumi, M. Mizumaki, and T. Kaambre, Phys. Rev. B **79**, 4 (2009).
17. H. Ikeno, F. M. F. de Groot, E. Stavitski, and I. Tanaka, J. Phys. Cond. Matt. **21**, 104208 (2009).
18. M. Haverkort, (priv. comm.) (2009).
19. A. Juhin, G. Calas, D. Cabaret, L. Galoisy, and J. L. Hazemann, Phys. Rev. B **76** (2007).
20. F. M. F. de Groot, J. C. Fuggle, B. T. Thole, and G. A. Sawatzky, Phys. Rev. B **41**, 928 (1990).
21. F. M. F. de Groot, J. C. Fuggle, B. T. Thole, and G. A. Sawatzky, Phys. Rev. B **42**, 5459 (1990).
22. F. de Groot, Coord. Chem. Rev. **249**, 31 (2005).
23. F. M. F. de Groot, J. Elec. Spec. **67**, 529 (1994).

24. R. K. Hocking, E. C. Wasinger, F. M. F. de Groot, K. O. Hodgson, B. Hedman, and E. I. Solomon, J. Am. Chem. Soc. **128**, 10442 (2006).
25. W. M. Heijboer, et al., J. Phys. Chem. B **107**, 13069 (2003).
26. P. Gambardella, et al., Nature Materials **8**, 189 (2009).
27. C. Piamonteze, F. M. F. de Groot, H. C. N. Tolentino, A. Y. Ramos, N. E. Massa, J. A. Alonso, and M. J. Martinez-Lope, Phys. Rev. B **71**, 020406 (2005).
28. E. C. Wasinger, F. M. F. de Groot, B. Hedman, K. O. Hodgson, and E. I. Solomon, J. Am. Chem. Soc. **125**, 12894 (2003).
29. F. M. F. de Groot, M. Grioni, J. C. Fuggle, J. Ghijsen, G. A. Sawatzky, and H. Petersen, Phys. Rev. B **40**, 5715 (1989).
30. T. Glaser, B. Hedman, K. O. Hodgson, and E. I. Solomon, Acc. Chem. Res. **33**, 859 (2000).
31. M. Wilke, F. Farges, P. E. Petit, G. E. Brown, and F. Martin, Am. Miner. **86**, 714 (2001).
32. W. M. Heijboer, P. Glatzel, K. R. Sawant, R. F. Lobo, U. Bergmann, R. A. Barrea, D. C. Koningsberger, B. M. Weckhuysen, and F. M. F. de Groot, J. Phys. Chem. B **108**, 10002 (2004).
33. W. M. Heijboer, D. C. Koningsberger, B. M. Weckhuysen, and F. M. F. de Groot, Catal. Today **110**, 228 (2005).
34. W. Gawelda, M. Johnson, F. M. F. de Groot, R. Abela, C. Bressler, and M. Chergui, J. Am. Chem Soc. **128**, 5001 (2006).
35. E. de Smit, I. Swart, J.F. Creemer, G.H. Hoveling, M.K. Gilles, T. Tyliszczak, P.J. Kooyman, H.W. Zandbergen, C. Morin, B.M. Weckhuysen, F.M.F. de Groot, et al., Nature **456**, 222 (2008).
36. E. de Smit, I. Swart, J. F. Creemer, C. Karunakaran, D. Bertwistle, H. W. Zandbergen, F. M. F. de Groot, and B. M. Weckhuysen, Angew. Chem. **48**, 3632 (2009).
37. M. Finazzi, N. B. Brookes, and F. M. F. de Groot, Phys. Rev. B **59**, 9933 (1999).
38. L. Braicovich, et al., Phys. Rev. Letters **102** (2009).
39. P. Glatzel and U. Bergmann, Coord. Chem. Rev. **249**, 65 (2005).
40. F. de Groot, Chem. Rev. **101**, 1779 (2001).
41. G. Vankó, F.M.F. de Groot, S. Huotari, R. Cava, T. Lorenz, M. Reuther, arXiv:0802.2744 (2008).
42. F. de Groot, G. Vanko, and P. Glatzel, J. Phys. Cond. Matt. **21**, 104207 (2009)).
43. E. Suljoti and F. M. F. de Groot, et al. (unpublished results) (2009).
44. P. Glatzel, A. Mirone, S. G. Eeckhout, M. Sikora, and G. Giuli, Phys. Rev. B **77** (2008).
45. R. F. Pettifer, S. P. Collins, and D. Laundy, Nature **454**, 196 (2008).